Journal of the Korean Ceramic Society
https://doi.org/10.1007/s43207-023-00307-3

ORIGINAL ARTICLE

Synthesis of B4C powder via the carbothermal reduction and photoreduction of Cr(VI) on B4C under visible light irradiation

Ozcan Koysuren[1] · **Hafize Nagehan Koysuren**[2]

Received: 29 January 2023 / Revised: 28 March 2023 / Accepted: 14 April 2023

Abstract
The environmental problem caused by wastewater containing hexavalent chromium (Cr(VI)) is of great interest and photocatalytic technology has recently been recognized as a suitable method for dealing with wastes containing Cr(VI). In this study, boron carbide (B_4C) powders were synthesized through a carbothermal reduction process using a polymer precursor, polyvinyl borate (PVB), and boric acid. The synthesized B_4C powders were studied as a photocatalyst for the removal of Cr(VI) from aqueous solutions under visible light irradiation. The effects of the B_4C seed crystals and the Ni catalyst on the crystal purity as well as the Cr(VI) photoreduction efficiency of the prepared B_4C powders were studied. B_4C, synthesized in the presence of both the B_4C seed crystals and the Ni catalyst, resulted in improved crystal purity, leading to an enhancement in the Cr(VI) photoreduction efficiency. The highest Cr(VI) removal rate of 65.1% was obtained. While the irradiation distance did not affect the Cr(VI) photoreduction efficiency much, the highest Cr(VI) removal was obtained with the visible light source (141 klux). The Cr(VI) removal rate was increased approximately 1.4 times with B_4C powders synthesized in the presence of both the B_4C seed crystals and the Ni catalyst. In addition, the effect of various parameters like the intial pH, Cr(VI) concentration and photocatalyst concentration on the Cr(VI) photoreduction efficiency of B_4C was examined. Within the scope of examining the recyclability of the prepared photocatalyst, the Cr(VI) removal rate of B_4C decreased from 65.1 to 52.4% after four consecutive cycles of Cr(VI) photoreduction experiments.

Keywords B_4C · Photocatalytic reduction · Cr(VI) removal · Carbothermal reduction · Visible light

1 Introduction

With the rapid increase in the human population in the last century, energy and environmental problems are becoming more prominent [1]. The earth is getting worse every day due to the continuous production of large volumes of solid/liquid/gas waste. Especially, the pollution of water resources has become one of the most prominent environmental pollution problems. Heavy metals like Cr, Hg, Ni, Pb, Cu, Mn and Ni are mostly found in industrial wastewaters discharged from metal mining, electrolysis, electroplating, smelting, refining, pharmaceutical and paint industries [2, 3]. The specified heavy metal ions are known as the most toxic inorganic pollutants both in soil and aquatic environments [3]. If the heavy metals mentioned are discharged freely into the environment within the industrial wastewater, they can be a serious source of pollution in water resources. Water contaminated with the heavy metals can cause denaturation and inactivation of enzymes and proteins in living cells, leading to serious damage to living things [2].

Environmental problems caused by Cr(VI) in wastewater have received more attention as Cr(VI) is both toxic and carcinogenic [2]. Most of the conventional Cr(VI) removal methods such as biological reduction [4], ion exchange [5], adsorption [6], electrocoagulation [7], chemical precipitation [8] and membrane filtration [9] suffer from the similar problems like high cost, low efficiency, complexity of the treatment process and the resulting secondary pollution. The photoreduction process has been considered as an alternative technique for the Cr(VI) removal. Highly toxic Cr(VI) ions can be reduced to less toxic Cr(III) ions using the photoreduction technique [10]. Although many semiconductors such as TiO_2 [11], B_2S_3 [12], CuO [13], CdS [14], ZnO [15],

✉ Ozcan Koysuren
koysuren@ankara.edu.tr

[1] Department of Energy Systems Engineering, Ankara University, 06830 Ankara, Turkey

[2] Department of Environmental Engineering, Kirsehir Ahi Evran University, 40100 Kirsehir, Turkey

Published online: 27 April 2023

ZrO_2 [16], g-C_3N_4 [10] and metal-organic framework [17] have been studied for the Cr(VI) photoreduction reaction, there is no study on the Cr(VI) photoreduction using B_4C as a photocatalyst.

Compared to mentioned photocatalysts, B_4C is more stable and environmentally friendly. To provide high photocatalytic activity, the conventional photocatalysts must be doped with noble metal atoms. The noble metal atoms form defect states between the conduction and valence band of the photocatalyst. The specified defect states act as trapping centers for the photoexcited electron or hole, leading to a suppression in the recombination of the photoexcited charge carriers and enhanced photocatalytic activity [18, 19]. The noble metal atoms also increase the amount of light absorbed [19]. B_4C has been known as an efficient photocatalyst under visible light without any noble metal dopants. B_4C has a relatively narrow band gap and exhibits a strong visible light response. B_4C can be a good alternative to the conventional semiconductor photocatalysts due to the mentioned features [20]. Apart from its photocatalytic property, B_4C is a diamond-like ceramic material with a high melting point, wear resistance, hardness and chemical stability. In addition, B_4C exhibits superior properties such as low density, high strength and high temperature resistance. B_4C has been used to produce wear resistant objects, hard coatings, light ceramic armor and cutting tools resistant to high temperature operations [21, 22]. B_4C is also an important construction material for aerospace applications [23].

B_4C in powder form can be synthesized by various techniques such as carbothermal reduction [24], ball milling [25], chemical vapor phase reaction [26], magnesiothermal reduction [27], pressureless sintering [28] and spark plasma sintering methods [29]. Among the specified techniques, the carbothermal reduction has received great attention due to its simplicity, low cost, high efficiency and large-scale production characteristics [30]. In the carbothermal reduction method, boric oxide is reduced by carbon to obtain B_4C powders [24]. However, the B_4C synthesis reaction mechanism is still unclear because of the lack of sufficient studies on this topic. In addition, the requirement of high process temperature, the difficulty of the process control and the purity of the resulting product are challenging issues to be overcome during the B_4C synthesis through the carbothermal reduction [24, 30].

Within the scope of the carbothermal reduction method, B_4C can be synthesized in powder form by using a polymer precursor through an exothermic reaction at relatively low temperatures [31–33]. In this context, Shawgi et al. (2017) synthesized the precursor polymer, polyvinyl borate (PVB) through the cross-linking reaction between polyvinyl alcohol and boric acid. After the heat treatment (~ 700 °C) of the precursor polymer, B_2O_3 and amorphous carbon phases are formed. With the continuation of the heat treatment (˃1100 °C), B_4C was obtained through the carbothermal reduction of the B_2O_3 phase [34]. In a different study, Kakiage et al. (2011) synthesized the PVB precursor polymer, including the B–O–C bond structure along its chain structure, through a dehydration reaction of boric acid and polyvinyl alcohol. The heat treatment of PVB led to the formation of the B_2O_3-carbon phases and then the B_4C structure at 1100–1300 °C by the carbothermal reduction reaction [35]. Similarly, the heat treatment of PVB to form the B_4C nanocrystals was reported by Yanase et al. and Mondal and Banthia [32, 33]. According to the studies from the literature, it is required to increase the heat treatment temperature above 1300 °C to obtain high crystal purity. High temperatures are required to activate the B_2O_3 and carbon phases to form nucleating points and to grow on the nucleating points through the carbothermal reaction to form large crystallites [36]. B_4C structures with low crystal purity were obtained at 1000–1100 °C. Different approaches have been applied in the literature to increase the crystalline purity of B_4C. da Rocha and de Melo [36] tried to synthesize B_4C nanocrystals from boric acid and amorphous carbon by carbothermal reduction reaction at 1750 °C. To increase the crystal purity of the product, B_4C seed crystals (0–5 wt%) were added into the reaction medium of B_4C. The B_4C seed crystals provided an increase in the crystal purity and a decrease in the nanocrystalline particle size [36]. Apart from the specified study, Aghaie et al. utilized the magnesiothermal reduction route to synthesize B_4C in powder form at 1050 °C and the addition of the B_4C seed crystals (2 wt%) enhanced the crystal purity [27]. In a different study, Yan et al. tried to increase the crystal purity by using metal catalysts such as (Fe, Co, Ni, Cu, and Zn). Among the metal catalysts tried, the Ni catalyst seemed to be effective to obtain mesoporous nanocrystals with high purity and surface area at 850° C [37].

In the present study, B_4C in powder form was obtained from the heat treatment of a polymer precursor, PVB, prepared though the condensation reaction of boric acid and polyvinyl alcohol. The B_4C seed crystal and the Ni catalyst were utilized to improve the crystal purity of the as-prepared B_4C. The Cr(VI) photoreduction efficiency of the B_4C samples was investigated. The effect of the B_4C seed crystals and the Ni catalyst on the Cr(VI) removal rate was studied. There is no study in literature on the Cr(VI) photoreduction efficiency of B_4C.

2 Experimental

2.1 Materials and methods

For the synthesis of boron carbide (B_4C), the precursor polymer, polyvinyl borate (PVB), was first synthesized

through the dehydration reaction of polyvinyl alcohol (PVA) and boric acid with a PVA/boric acid ratio of 4.2/1 (mol/mol). A certain amount of PVA (2.47 g) was dissolved in 50 ml of distilled water at 80 °C. At the same time, a certain amount of boric acid (according to the 4.2/1 mol ratio of PVA/boric acid) was dissolved in 50 ml of distilled water in a separate beaker. Then, the boric acid solution was added to the PVA solution and mixed at 80 °C. A gel structure formed within a few minutes after the boric acid solution was mixed with the PVA solution. The as-prepared gel was dried in an oven at 120 °C and then it was ground to powder. The powder sample was heated in a furnace at 1100 °C with a flow of Argon. Hence, pure B_4C in powder form was obtained [32]. To increase the crystal purity of the obtained product, B_4C seed crystals (0–5, wt%; 40–60 nm) and nickel catalyst ($Ni(NO_3)_2{\cdot}6H_2O$) (0–5, wt%) were added into the PVA solution prior to mixing with the boric acid solution [32, 36]. The same process steps applied to prepare the pure B_4C particles were also followed to prepare the B_4C particles synthesized in the presence of the B_4C seed crystals and the Ni catalyst. In addition, the final product was kept under stirring in concentrated HNO_3 solution for 1h and rinsed with distilled water to separate the Ni catalyst from B_4C (Fig. 1). The samples synthesized in the presence of 2.5 or 5 wt% B_4C seed crystals were named as B_4C(2.5,0) or B_4C(5,0), respectively. In addition, the samples prepared in the presence of 5 wt% B_4C seed crystals and 2.5 or 5 wt% Ni catalyst were named as B_4C(5,2.5) or B_4C(5,5), respectively.

2.2 Structural, morphological and optical characterization

Fourier-transform infrared (FTIR) spectroscopy of the B_4C samples was characterized using a Bruker IFS 66/S model spectrophotometer. The instrument utilized in X-ray diffraction (XRD) analysis was an Ultima IV model X-ray diffractometer manufactured by Rigaku. A QUANTA 400 F model field emission scanning electron microscope (FE-SEM) was used to investigate the particle morphology of the B_4C samples. The specific surface area and the pore structure of the B_4C samples were examined using the analysis of N_2 isotherms collected using a Autosorb-6 model analyzer (Quantachrome Corporation) according to the Brunner–Emmett–Teller (BET) method and the Barret-Joyner-Halender (BJH) method, respectively. The UV–Vis absorption spectroscopy of the B_4C samples was characterized using a Genesys 10 S model UV–Vis spectrophotometer (Thermo Scientific).

2.3 Characterization of the Cr(VI) photoreduction performance

The Cr(VI) photoreduction experiment was carried out in a 100 ml beaker at room temperature. The Cr(VI) solution (20 mg/l $K_2Cr_2O_7$ solution) was prepared by dissolving 1 mg of $K_2Cr_2O_7$ in 50 ml distilled water. 25 mg of the B_4C sample was added to the as-prepared Cr(VI) solution and kept in the dark for half an hour to establish an adsorption-desorption equilibrium. After the adsorption-desorption equilibrium was achieved, the Cr(VI) solution was exposed to the

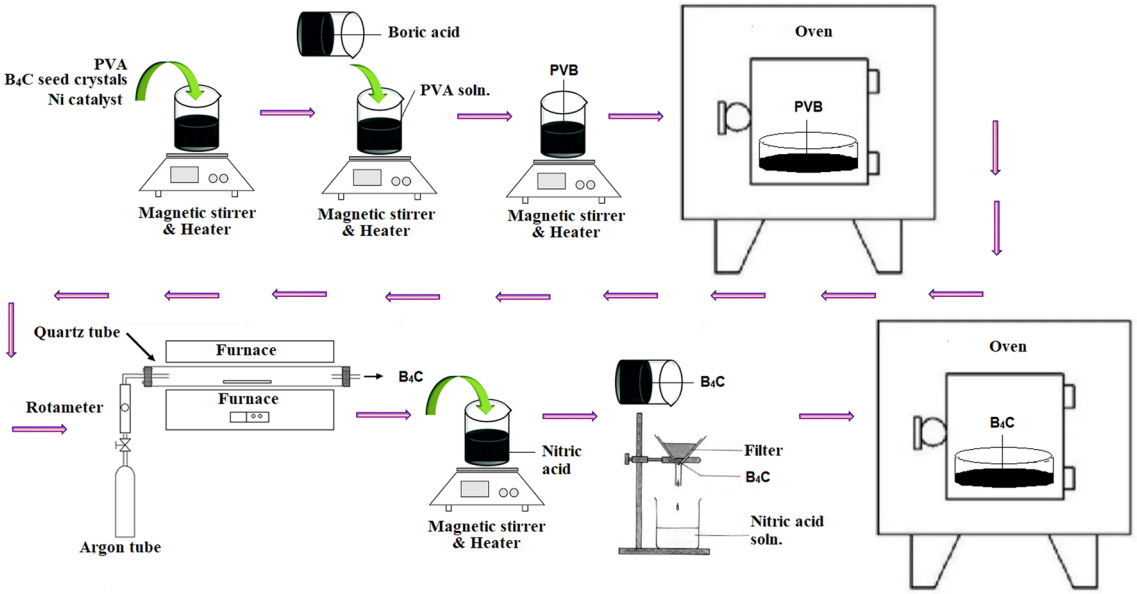

Fig. 1 Schematic diagram for the synthesis of B_4C powders

visible light irradiation (380–750 nm, 300 W). The reaction system was ventilated with air to prevent overheating of the Cr(VI) solution. To examine the effects of the light source on the photoreduction efficiency, UVC (254 nm, 30 W), UVA (340 nm, 12 W) lamps and natural sunlight (June–August, 11.00–14.00) were also used as alternatives to the visible light lamp. The distance between the visible light lamp and the solution was kept as 10 cm. In addition, to examine the effect of the radiation distance, the distance between the visible light lamp and the Cr(VI) solution was changed to 5 and 15 cm, respectively. The intensity of the incoming light was measured using a lux meter (CEM DT-1308). At a certain time interval (20 min), a sample was taken from the Cr(VI) solution and the Cr(VI) concentration was determined using the diphenylcarbazide (DPC) spectrophotometric method [38]. The Cr(VI) concentration was determined by UV–Vis spectrophotometer (Genesys 10 S, Thermo Scientific). The photoreduction efficiency of Cr(VI) was calculated using the absorption data of the Cr(VI)-diphenylcarbazide complex at 543 nm according to the following equation [24, 38]:

$$\text{Photoreduction efficiency } (\%) = \left(C_0 - C_t\right)/C_0 \times 100\% \quad (1)$$

In addition, the conformity of the Cr(VI) photoreduction reaction to the pseudo-first-order kinetic model was investigated using the following equation [24, 39]:

$$\ln\left(C_0/C_t\right) = kt \quad (2)$$

where C_0 and C_t correspond to the initial and the final concentration of the Cr(VI) solution, respectively [24, 39]. The reaction rate constant (k) was determined from the slope of the ln(C_0/Ct) vs. time graph from 0 to 120 min. Scavenger experiments were conducted to verify the active mobile charge carrier for the Cr(VI) photoreduction and study the possible photoreduction mechanism of Cr(VI) on B_4C. For this purpose, potassium persulfate (1 mM) and ammonium oxalate (1 mM) were introduced into the Cr(VI) solution of B_4C(5,2.5) to capture the photogenerated electrons and holes of B_4C, respectively. To study the effect of the initial pH of the Cr(VI) solution, the current pH of the Cr(VI) solution was adjusted to 4 and 10 by using 1 M HCl solution and 1 M NaOH solution, respectively. The effect of the initial Cr(VI) concentration on the Cr(VI) photoreduction efficiency of B_4C(5,2.5) was studied by changing $K_2Cr_2O_7$ concentration of the solution to 10 and 30 mg/l, respectively. Also, to examine the potential effect of the photocatalyst concentration on the Cr(VI) removal rate, the B_4C(5,2.5) concentration was adjusted to be 0.1 and 1.0 g/l, respectively. To examine the recyclability of the prepared photocatalyst, the B_4C(5,2.5) sample was separated from the Cr(VI) solution following the photoreduction experiment. It was then rinsed with distilled water, dried and reused for another Cr(VI) photoreduction experiment.

3 Results and discussion

3.1 FTIR analysis

During the heat treatment of the polymer precursor, PVB, micron-sized B_2O_3 particles dispersed in an amorphous carbon phase was obtained. The following reaction step at which the B_4C phase is formed is the carbothermal reduction of boron oxide (3) [35]:

$$2B_2O_3 + 7C \leftrightarrow B_4C + 6CO \quad (3)$$

The FTIR spectrum of B_4C(0,0) illustrates characteristic peaks of B_4C at 570 and 547 cm^{-1}, attributed to the C–B–C bending vibrations (Fig. 2a) [35]. The same spectrum exhibits characteristic peaks at 644, 715, 884 and 1194 cm^{-1}, which were assigned to the B–C stretching vibrations [40, 41]. The presence of the peaks of B–C and C–B–C bonds confirms the successful conversion of the polymer precursor, polyvinyl borate, to B_4C through the carbotermal reduction of B_2O_3 [35, 40]. In addition, there are transmittance peaks at 3210, and 1742 cm^{-1}, which were attributed to the stretching vibrations of –OH and C=O bonds, respectively [40, 42]. The peaks at 1449 and 1379 cm^{-1} were assigned to the stretching vibrations of B–O bonds at the B_4C surface [41, 42]. The polymer precursor, PVB, was synthesized through the condensation reaction between boric acid and PVA to form B–O–C bonds on its chain structure. The absence of the peaks at 1287 and 1130 cm^{-1}, belonging to the stretching vibrations of B–O–C bonds, might also confirm the successful conversion of PVB to B_4C [42].

B_4C(5,0) was synthesized in the presence of the B_4C seed crystals (5 wt%). Compared to B_4C(0,0), there was a significant increase in the intensity of transmittance peaks seen on the FTIR spectrum of B_4C(5,0) (Fig. 2b). In particular, the increase in the intensity of the transmittance peaks observed at 547, 715, 884 and 1194 cm^{-1} showed that the

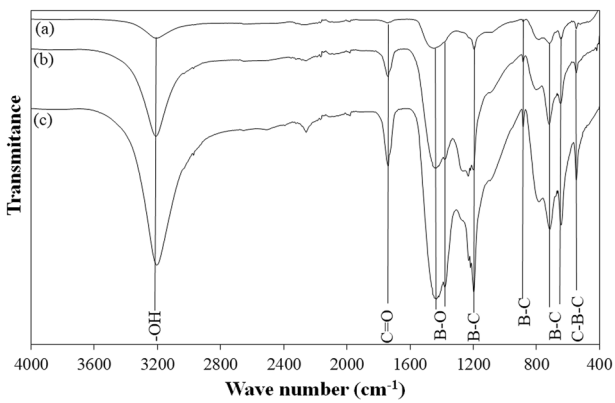

Fig. 2 FTIR spectrum of **a** B_4C(0,0), **b** B_4C(5,0) and **c** B_4C(5,2.5)

B_4C structure was better formed in the presence of the B_4C seed crystals. Unlike $B_4C(0,0)$, there is a transmittance peak on the FTIR spectrum of $B_4C(5,0)$ at 1231 cm^{-1}, attributed to the icosahedral vibrations of B_4C [43]. $B_4C(5,2.5)$ was synthesized in the presence of the Ni catalyst (2.5 wt%) in addition to the B_4C seed crystals (5 wt%). Compared to $B_4C(0,0)$ and $B_4C(5,0)$, the increase in the intensity of characteristic transmittance peaks of B_4C at 547, 644, 884 and 1194 cm^{-1} is important in terms of the purity of the as-prepared product and the success of the synthesis reaction (Fig. 2c). The B–C bond structure of B_4C might grow more successfully in the presence of both the B_4C seed crystals and the Ni catalyst.

4 XRD analysis

On the XRD diffractogram of $B_4C(0,0)$ (Fig. 3a), there are diffraction peaks at 21.9°, 23.4°, 31.8°, 34.9°, 37.8°, 39.1°, 53.4°, 61.7°, 63.6°, 64.5°, 66.6°, 70.3°, 71.2°, 71.7° and 75.3°, which can be indexed to (003), (012), (110), (113), (021), (113), (205), (303), (125), (018), (220), (131), (223), (312) and (306) planes of the rhombohedral B_4C phase (JCPDS No. 26–232). According to Fig. 3a, B_4C crystal phase is presented with trace amount of amorphous carbon phase and B_2O_3 crystal phase. The broad peak seen in the diffraction angle of 20–30° on the XRD spectrum of $B_4C(0,0)$ was attributed to the amorphous carbon phase and the diffraction peak at 27.8° was attributed to the B_2O_3 crystal structure [35]. According to the literature, the heat treatment of the polymer precursor, PVB, between 600–700° C leads to the formation micron-sized B_2O_3 particles dispersed in an amorphous carbon phase. Further heat treatment above 1100° C results in conversion of the B_2O_3 and carbon phases to the B_4C structure through the carbothermal reduction reaction [35]. The sharp diffraction peaks seen on the XRD spectrum of $B_4C(0,0)$ indicated the crystallinity of the product prepared in the absence of the B_4C seed crystals and the Ni catalyst (Fig. 3a). On the other hand, the diffraction peaks belonging to the B_2O_3 and amorphous carbon phases indicated that not all of the reactants were converted to the B_4C structure.

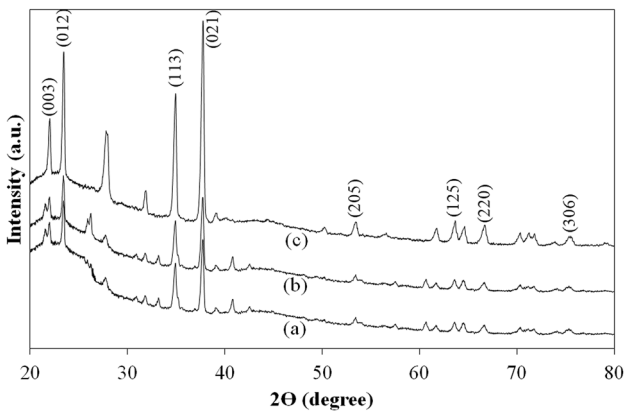

Fig. 3 XRD diffractogram of **a** $B_4C(0,0)$, **b** $B_4C(5,0)$ and **c** $B_4C(5,2.5)$

When the B_2O_3 phase is in contact with the amorphous carbon phase, the reaction starts with the nucleation step, which is based on the activation of reactants. Then, the as-prepared nuclei start to grow through the chemical reaction of the reactants. At relatively low temperatures, a few nuclei can be formed, leading to formation of large crystallites. Increasing the nucleation points results in the formation of many small crystallites [36]. In addition, a catalyst can lower the activation energy of the nucleation step, leading to the formation of a highly crystalline structure with small crystallites in a short time [37]. According to Fig. 3, the intensity of the diffraction peaks seen on the XRD spectrum of $B_4C(5,0)$ and $B_4C(5,2.5)$ was higher than that of $B_4C(0,0)$. Both the B_4C seed crystals and the Ni catalyst appear to improve the crystallinity of the as-prepared B_4C. In addition, both the B_4C seed crystals and the Ni catalyst might favor to the formation of the nucleation points, giving rise to smaller B_4C crystallites. The B_4C crystal purity of the as-prepared product was estimated using the peak intensity ratio (4) [35]:

$$B_4C \text{ crystal purity } (\%) = I_{B4C} / I_{B4C} + I_C + I_{B2O3} \times 100 \quad (4)$$

where I_{B4C} is the main peak intensity of B_4C ($2\theta = 37.8°$), I_C is the peak intensity of the amorphous carbon phase ($2\theta = 26°$) and I_{B2O3} is the peak intensity of the B_2O_3 crystal structure ($2\theta = 27.8°$) [35]. According to the peak intensity ratio, the crystal purity of $B_4C(0,0)$ increased from 34.4 to 42.8% and 55.2% with $B_4C(5,0)$ and $B_4C(5,2.5)$, respectively. The mean crystallite size (Dp) of $B_4C(0,0)$, $B_4C(5,0)$ and $B_4C(5,2.5)$, calculated using the Scherrer equation (5), was found out to be 31.11 , 28.77 and 28.71 nm, respectively.

$$Dp = (0.94\ \lambda) / (\beta\ Cos\theta) \quad (5)$$

where Dp is the mean crystallite size, λ is the X-ray wavelength, β is the full width at half maximum intensity of the main diffraction peak and θ is the Braggs' angle [44].

5 N_2 adsorption-desorption study

Figure 4 illustrates N_2 adsorption and desorption isotherm curve for $B_4C(0,0)$, $B_4C(5,0)$ and $B_4C(5,2.5)$. The Barret–Joyner–Halender (BJH) curve of the samples is also shown in Fig. 4, revealing that all of the samples exhibited relatively narrow pore size distribution, and mesopores were generated on the samples. Also, all of the samples exhibit a type IV isotherm [45]. According to BJH curves, the mean

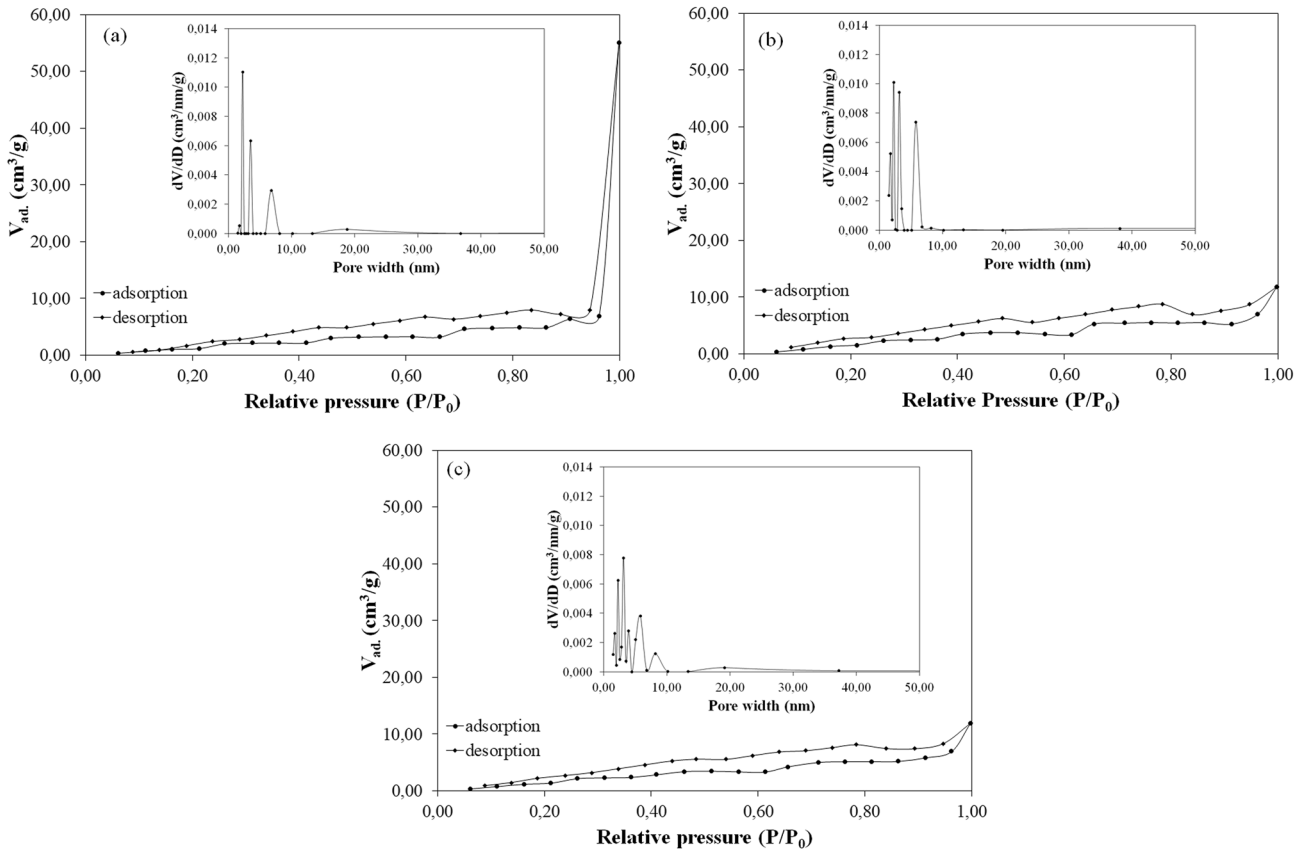

Fig. 4 N_2 adsorption–desorption isotherm (Inset plots exhibit the BJH pore size distribution) for **a** $B_4C(0,0)$, **b** $B_4C(5,0)$ and **c** $B_4C(5,2.5)$

pore size of $B_4C(0,0)$, $B_4C(5,0)$ and $B_4C(5,2.5)$ was found out to be 2.25, 2.25 and 2.75 nm, respectively. In addition, the pore volume of $B_4C(0,0)$, $B_4C(5,0)$ and $B_4C(5,2.5)$ was calculated as 0.087, 0.025 and 0.026 cm^3/g, respectively. While no significant effect of the B_4C seed crystals and the Ni catalyst was observed on the mean pore size of B_4C—a significant reduction in the pore volume was observed with B_4C synthesized in the presence of the B_4C seed crystals and the Ni catalyst. The BET analysis of the B_4C samples indicated surface area values close to each other. The surface area was found out to be 14.0, 16.5 and 13.7 m^2/g for $B_4C(0,0)$, $B_4C(5,0)$ and $B_4C(5,2.5)$, respectively.

A typical Cr(VI) photoreduction reaction consists of three steps. First, the photocatalyst absorbs the incoming light. Then, the photoexcited charge carriers are generated in the bulk of the photocatalyst and they transfer to the photocatalyst surface. Finally, the photoexcited charge carriers react with the Cr(VI) ions adsorbed on the photocatalyst surface [46]. Therefore, an enlarged surface area and pore diameter are advantageous in terms of the Cr(VI) photoreduction performance. A photocatalyst with an enlarged surface can absorb more Cr(VI) ions on its surface, leading to an increase in the amount of reactive sites on the photocatalyst. Yin et al. [46] studied the effect of the specific surface area on the Cr(VI) photoreduction rate. When the specific surface of the prepared photocatalyst increased from 19.3 to 34.5 m^2/g, the Cr(VI) removal rate increased from 86.3 to 99.1% [46]. In another study, Challagulla et al. [47] also obtained an enhancement in the Cr(VI) removal rate with an enlarged surface area. The composite photocatalyst completely reduced Cr(VI) 40 min earlier when the specific surface area of the photocatalyst was enlarged from 11.9 to 32.6 m^2/g [47]. No significant difference was observed in the surface area values of the B_4C photocatalysts produced within the scope of this study. Therefore, the effect of the specific surface area on the Cr(VI) photoreduction efficiency of B_4C was expected to be negligible.

6 Morphological analysis

According to the FE-SEM images of $B_4C(0.0)$, B_4C crystal structures were formed in the range of 1–10 µm (Fig. 5a). Besides the B_4C crystal structures, there are also layers thought to belong to the amorphous carbon phase, indicating that not all of the amorphous carbon phase was converted to the B_4C phase at 1100° C without using the B_4C seed crystals and the Ni catalyst. The FE-SEM images of

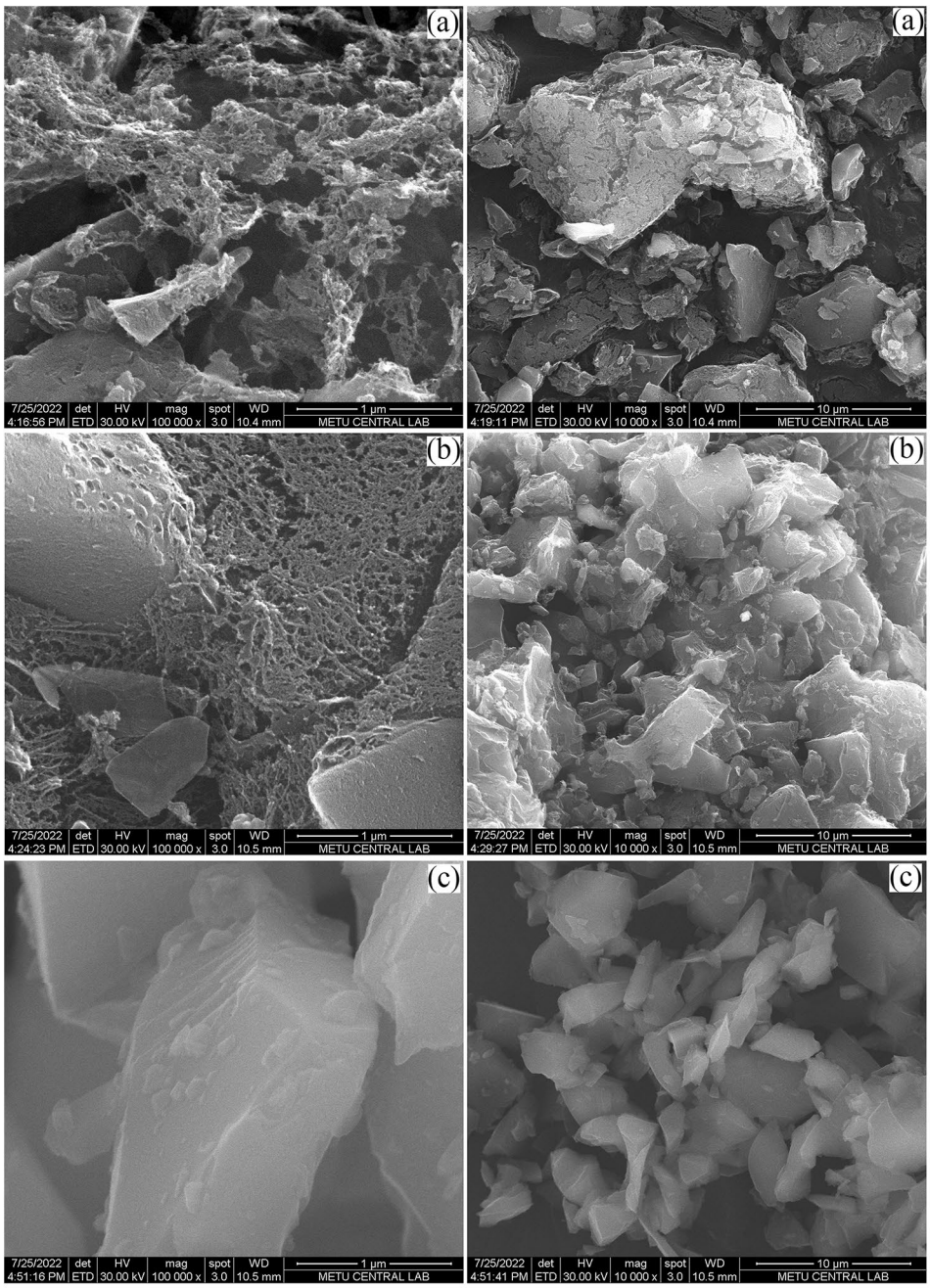

Fig. 5 FE-SEM images of **a** $B_4C(0,0)$, **b** $B_4C(5,0)$ and **c** $B_4C(5,2.5)$

$B_4C(5,0)$ and $B_4C(5,2.5)$ are similar to each other. Unlike $B_4C(0,0)$, there are more crystal structures in the range of 1–5 µm on the FE-SEM images of both $B_4C(5,0)$ and $B_4C(5,2.5)$ (Fig. 5b, c). Especially, more homogenous and smaller crystal structures were obtained with B_4C synthesized in the presence of both the B_4C seed crystals and the Ni catalysts (Fig. 5c). The B_4C seed crystals might act as additional nucleating points during the carbotermal reduction reaction between the carbon and B_2O_3 phases, leading to the formation of smaller and more crystal structures. In addition to the B_4C seed crystals, Ni catalyst might lower the activation energy of the nuclei formation, resulting in the formation more smaller B_4C crystals.

7 UV–visible absorption study

Figure 6 shows the UV–Vis absorption spectrum of the as-prepared samples. All of the B_4C samples exhibited strong absorption in both the UV light region (225–350 nm) and the visible light region (600–800 nm), which might be assigned to the mid-gap energy states of B_4C. The

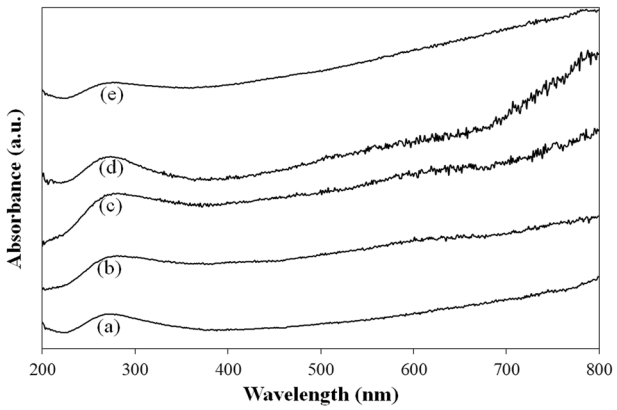

Fig. 6 UV–Vis absorption spectrum of **a** $B_4C(0,0)$, **b** $B_4C(2.5,0)$ **c** $B_4C(5,0)$, **d** $B_4C(5,2.5)$ and **e** $B_4C(5,5)$

specified mid-gap energy states might induce both the deep level and indirect inter-band transitions [48]. The light absorption ability is important in terms of the formation of the photogenerated charge carriers and the related Cr(VI) photoreduction reaction. The incoming light must be absorbed by B_4C to excite its valence band electrons to the conduction band to generate the photoexcited electron-hole pair. There is no significant difference in the UV–Vis absorption spectrum of the samples. Considering the light absorption ability, all of the B_4C samples seem to be suitable for the Cr(VI) photoreduction study in the wavelength range of 200–800 nm.

The Tauc plots exhibited in Fig. 7 were derived from the UV–Vis absorption spectrum of the samples using the following formula (6):

$$(\alpha hv)^2 = A\left(hv - E_g\right) \tag{6}$$

where α is the optical absorption coefficient, A is a constant, hv is the photon energy of the incoming light and E_g is the optical band gap energy [49]. Based on the extrapolation of the curve on the Tauc plots (Fig. 7), the optical band gap energy of $B_4C(0,0)$, $B_4C(2.5,0)$, $B_4C(5,0)$, $B_4C(5,2.5)$ and $B_4C(5,5)$ was 2.15 , 2.10 , 2.10 , 2.05 and 2.05 eV, respectively. Although the B_4C seed crystals and the Ni catalyst enhanced the crystal structure and lower the mean crystallite size, they did not have a determinant effect on the optical band gap energy. The optical band gap energy of the samples was roughly the same.

8 Photocatalytic activity

Figure S1 illustrates the absorption changes of the Cr(VI)-diphenylcarbazide complex during the photoreduction reaction in the presence of $B_4C(0,0)$ under four different light sources (UVC, UVA, natural sun light and visible light). When the light sources were compared, a greater decrease in the peak intensity of the absorption spectrum was detected under visible light. The measured intensity of the light sources for UVC, UVA, natural sun light and visible light was 450 lux, 220 lux, 101 klux and 141 klux, respectively. Both the natural sun light region (12.4 eV -1.2×10^{-3} eV) and the visible light region (1.5–3.1 eV) seemed to be more suitable for $B_4C(0,0)$ in terms of the light absorption ability (Eg = 2.15 eV). The highest value in terms of the light intensity was obtained with the visible light source. A reduction in the absorbance at 543 nm on the plot of absorption vs.

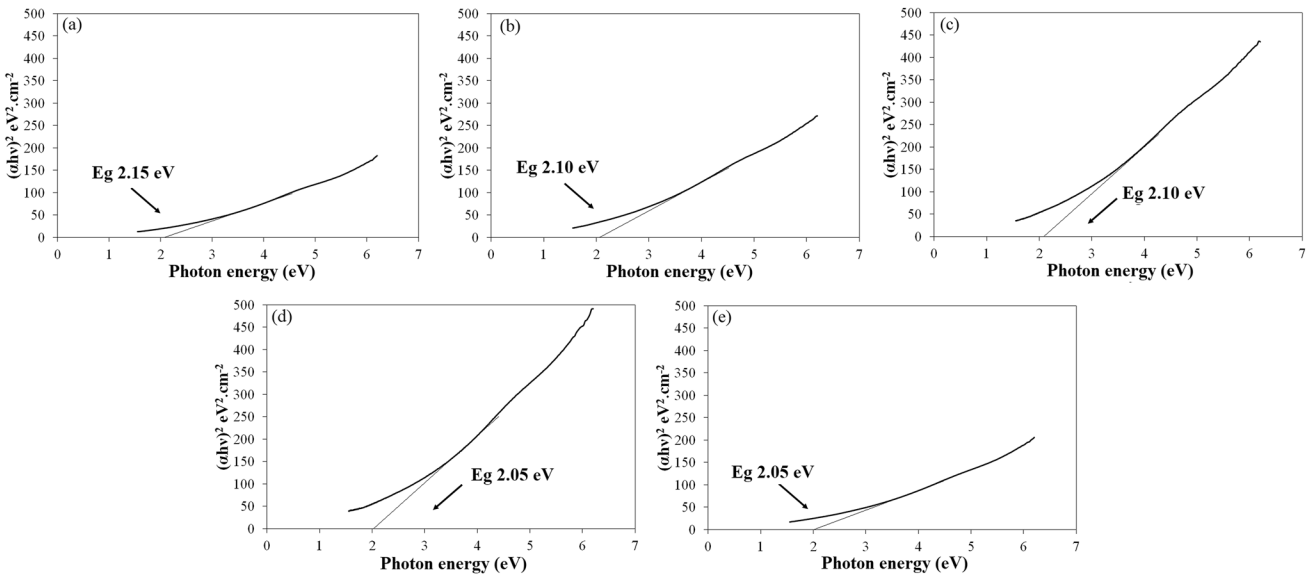

Fig. 7 Tauc plots for **a** $B_4C(0,0)$, **b** $B_4C(2.5,0)$ **c** $B_4C(5,0)$, **d** $B_4C(5,2.5)$ and **e** $B_4C(5,5)$

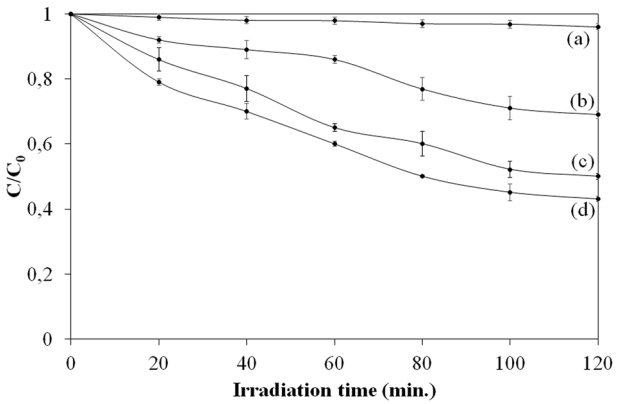

Fig. 8 The Cr(VI) photoreduction rate in the presence of $B_4C(0,0)$ under **a** UVC, **b** UVA, **c** natural sunlight and **d** visible light irradiations

wavelength reflects the Cr(VI) photoreduction on the sample. Then, it was utilized as a measure of the Cr(VI) photoreduction efficiency. The Cr(VI) photoreduction efficiency was found out to be 4.1, 31.1, 50.0 and 56.9% with $B_4C(0,0)$ under UVC, UVA, natural sunlight and visible light sources, respectively (Fig. 8). This finding revealed that the Cr(VI) photoreduction efficiency of B_4C is highly dependent on the light intensity and the wavelength range of the light source. When the natural sun light and the visible light lamp were used, B_4C could absorb more of the incoming light due to its relatively narrow optical band gap. The amount of the incident photons absorbed by B_4C is important to obtain an enhanced Cr(VI) photoreduction efficiency [50]. The highest Cr(VI) photoreduction efficiency was obtained under the visible light source. Hence, it was utilized as the light source in the following parts of the Cr(VI) photoreduction study.

The effect of the light intensity on the Cr(VI) photoreduction efficiency was studied by changing the distance between the light source and the Cr(VI) solution. Figure S2 exhibits the absorption changes of the Cr(VI)-diphenylcarbazide complex during the Cr(VI) photoreduction reaction with $B_4C(0,0)$ when the distance between the visible light lamp and the Cr(VI) solution was kept at three different values. Reducing the distance between the light source and the Cr(VI) solution from 15 to 10 cm caused a decrease in the peak intensity of the absorption spectrum. However, reducing the irradiation distance from 10 to 5 cm caused a slight increase in the peak intensity of the absorption spectrum (Figure S2). The light intensity is inversely proportional to the square of the radiation distance. As the radiation distance increases, the light intensity decreases [51]. As expected, decreasing the distance between the light source and the Cr(VI) solution from 15 to 10 cm and 5 cm increased the light intensity from 39 klux to 141 lux and 262 klux, respectively. On the other hand, the photocatalytic activity of semiconductors varies for different intensities of light. The Cr(VI) photoreduction rate increases with increasing the intensity of the light at a low light intensity (0–25 klux). The Cr(VI) photoreduction rate depends on the square root of the intensity of the incoming light at an intermediate light intensity (˃ 32 klux). A high-intensity light irradiation reduces the Cr(VI) photoreduction rate due to the promotion of the photoexcited electron-hole recombination [52]. When the distance between the light source and the Cr(VI) solution was reduced from 15 to 10 cm and 5 cm, the Cr(VI) removal rate for $B_4C(0,0)$ changed from 53.1 to 56.9% and 55.5%, respectively (Fig. 9). Changing the radiation distance from 15 to 10 cm slightly enhanced the Cr(VI) removal rate, indicating that the light intensity changed within the intermediate light intensity range. On the other hand, reducing the radiation distance from 10 cm to 5 cm slightly regressed the Cr(VI) photoreduction rate, indicating that the light intensity reached to the high-intensity light region. Thus, the radiation distance of 10 cm, providing the highest Cr(VI) removal rate, was utilized in the following parts of the Cr(VI) photoreduction study.

Figure S3 shows absorbance changes of Cr(VI)-diphenylcarbazide complex in the presence of the B_4C samples. The absorbance of the Cr(VI)-diphenylcarbazide complex with $B_4C(2.5,0)$ and $B_4C(5,0)$ was lower than that of $B_4C(0,0)$. In addition, the absorbance of the Cr(VI)-diphenylcarbazide complex with $B_4C(5,2.5)$ and $B_4C(5,5)$ was lower than that of the remaining samples. Figure 10 illustrates the Cr(VI) photoreduction rate of the samples under the visible light irradiation. The Cr(VI) removal rate by $B_4C(0,0)$, $B_4C(2.5,0)$ and $B_4C(5,0)$ were 56.9, 58.7 and 59.4%, respectively. According to the XRD analysis, the crystal purity of B_4C increased with the B_4C seed crystals, added into the reaction medium during the polymer precursor synthesis. A low crystal purity is expected to form structural defects, behaving as active sites for the recombination of the photogenerated charge carriers. A high crystal purity can promote

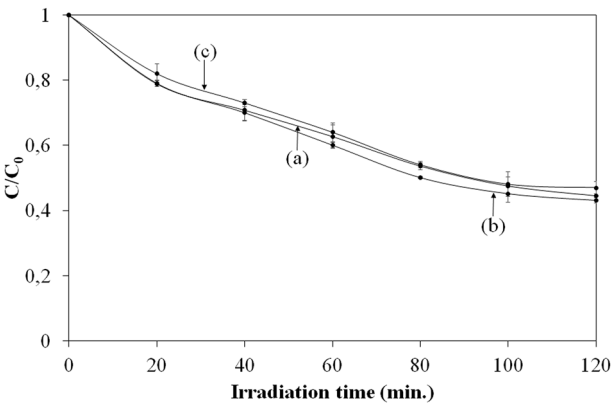

Fig. 9 The Cr(VI) photoreduction rate in the presence of $B_4C(0,0)$ with different radiation distance between the visible light source and the Cr(VI) solution: **a** 5 cm, **b** 10 cm and **c** 15 cm

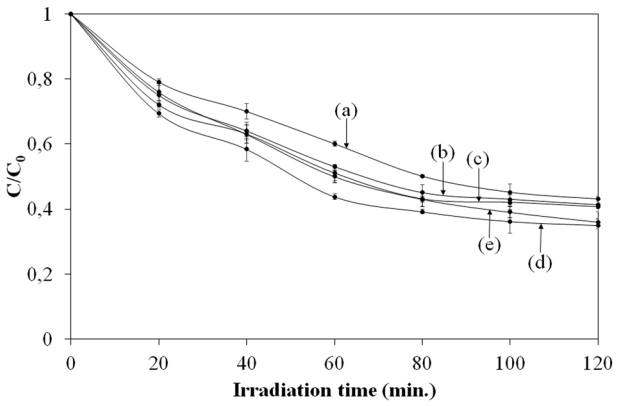

Fig. 10 The Cr(VI) photoreduction rate in the presence of **a** $B_4C(0,0)$, **b** $B_4C(2.5,0)$ **c** $B_4C(5,0)$, **d** $B_4C(5,2.5)$ and **e** $B_4C(5,5)$

the transfer of the photoexcited electron-hole pair from the center of the semiconductor to the surface, where the Cr(VI) photoreduction reaction takes place. Hence, a high crystal purity is important in terms of an enhanced photocatalytic activity [53]. The improvement in the Cr(VI) photoreduction efficiency with $B_4C(2.5,0)$ and $B_4C(5,0)$ was attributed to the improvement in the crystal purity. The Cr(VI) removal rate by $B_4C(5,2.5)$ and $B_4C(5,5)$ were found out to be 65.1 and 63.9%, respectively. According to the XRD analysis, the crystal purity of B_4C also increased with the Ni catalyst, added into the reaction medium with the B_4C seed crystals during the polymer precursor synthesis. The reason for the enhancement in the Cr(VI) removal rate was also attributed to the increase in the crystal purity of B_4C with the Ni catalyst. The highest Cr(VI) removal rate was obtained by $B_4C(5,2.5)$ (Fig. 10). A control experiment was also conducted with $B_4C(0,0)$ to check both the oxidant effect of the Cr(VI) ion source, $K_2Cr_2O_7$, and the surface adsorption effect of Cr(VI) on the photocatalyst. For this purpose, the Cr(VI) photoreduction experiment was performed in the dark in the absence of the visible light source. According to Figure S4, the Cr(VI) removal rate in the presence of $B_4C(0,0)$ decreased from 56.9 to 4.0% within 120 min when there was no visible light irradiation. Compared with the oxidant effect of $K_2Cr_2O_7$ and the surface adsorption effect of Cr(VI) on the photocatalyst, it was observed that the photoreduction effect was more dominant in the removal of Cr(VI) from the aquatic solution.

The reaction rate constants, derived from Figure S5, are shown on Table 1. According to Table 1, the addition of the B_4C seeds crystals into the reaction of medium of PVB increased the reaction rate. In addition, the Cr(VI) photoreduction rate increased with the addition of the Ni catalyst into the reaction medium. The reaction rate constant for $B_4C(5,0)$ was almost 1.2 times higher than that of $B_4C(0,0)$. When compared with $B_4C(0,0)$, an almost 1.4-fold increase

Table 1 Adjusted parameters of the pseudo-first order kinetic model

Sample	k (min^{-1})	R^2
$B_4C(0,0)$	0.0078	0.9594
$B_4C(2.5,0)$	0.0087	0.8891
$B_4C(5,0)$	0.0090	0.8547
$B_4C(5,2.5)$	0.0105	0.8571
$B_4C(5,5)$	0.0096	0.9410

was obtained by $B_4C(5, 2.5)$ in the reaction rate constant. The reaction rate constants resulted in high R^2 values close to 1, indicating that the Cr(VI) photoreduction data were in agreement with the pseudo-first-order kinetic model.

Upon exposure to the visible light, electrons in the valence band of B_4C are excited to the conduction band, leading to the formation of the photoexcited holes in the valence band and the photoexcited electrons in the conduction band (7).

$$B_4C + hv \rightarrow e^- + h^+ \quad (7)$$

The photogenerated electron-hole pairs move to the surface of B_4C. Electrons reaching the surface of B_4C can reduce Cr(VI) to Cr(III). The reduction reaction of Cr(VI) to Cr(III) in a neutral reaction medium is expected to occur according to the following reaction (8) [54]:

$$Cr_2O_7^{2-} + 14H^+ + 6e^- \rightarrow 2Cr^{3+} + 7H_2O \quad (8)$$

According to the normal hydrogen electrode (NHE), the reduction potential of $Cr_2O_7^{2-}$ to Cr (III) is 1.33 eV. The redox potential of the $Cr_2O_7^{2-}$/Cr (III) couple is more positive than the conduction band potential of B_4C (Fig. 11) [54, 55]. According to NHE, the reduction potential of O_2 to the superoxide radical ($\cdot O^{2-}$) is −0.33 eV. This value is also more positive than the conduction band potential of B_4C (Fig. 11) [56].

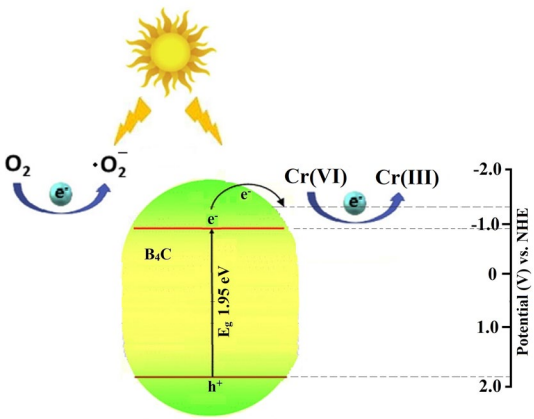

Fig. 11 Proposed photoreduction mechanism of Cr(VI) on B_4C

Due to the indicated potential difference, O_2 molecules can also be reduced with the photogenerated electrons of B_4C (9).

$$O_2 + e^- \rightarrow \cdot O_2^- \quad (9)$$

On the other hand, the photogenerated holes cannot oxidize H_2O molecules to the hydroxyl (·OH) radical (10) since the H_2O/·OH redox potential (2.27 eV) relative to NHE is more positive than the valence band potential of B_4C (Fig. 11) [55, 56].

$$H_2O + h^+ \rightarrow \cdot OH + H^+ \quad (10)$$

According to the band potential of B_4C and the reduction potential of the Cr(VI)/Cr(III) couple, it was estimated that only the photogenerated electrons are effective in the photoreduction reaction of Cr(VI). Scavenger experiments were also conducted to verify the active mobile charge carriers for the Cr(VI) photoreduction. Potassium persulfate and ammonium oxalate were added separately to the Cr(VI) solution as electron-hole scavengers. With the addition of potassium persulfate as an electron scavenger, the Cr(VI) photoreduction rate of B_4C(5,2.5) reduced from 65.1 to 50.9% in 120 min under visible light (Fig. 12a), revealing the significance of the photoinduced electrons in the Cr(VI) photoreduction. On the other hand, the introduction of ammonium

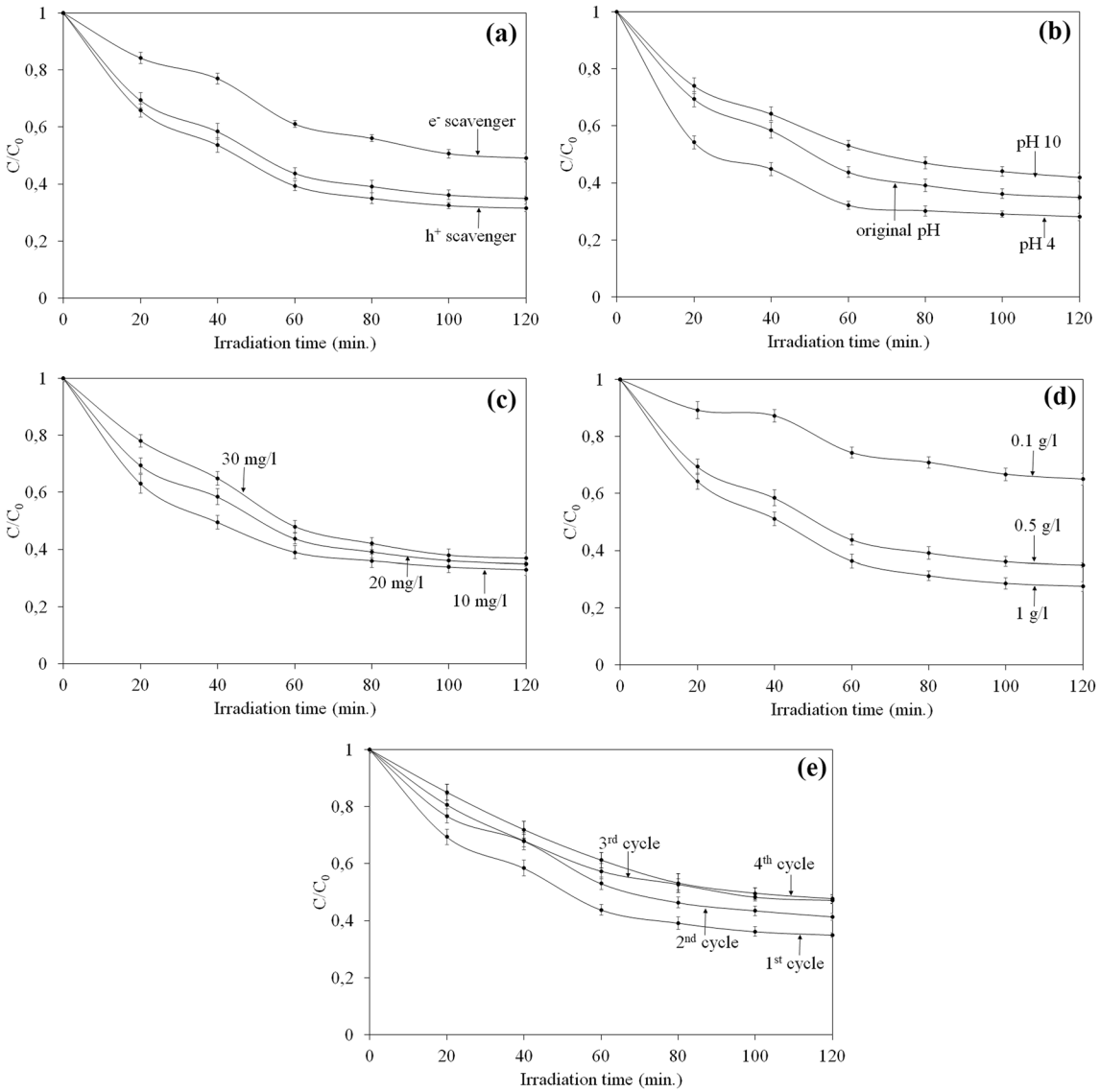

Fig. 12 Effect of **a** electron (e^-) and hole (h^+) scavengers, **b** the initial pH of the Cr(VI) solution, **c** the initial Cr(VI) concentration of the solution, **d** the initial photocatalyst concentration, **e** recyclability of the photocatalyst on the Cr(VI) photoreduction rate of B_4C(5,2.5) under visible light irradiation

oxalate as a hole scavenger into the Cr(VI) solution enhances slightly the Cr(VI) removal rate of B_4C(5,2.5) from 65.1 to 68.4% in 120 min under visible light (Fig. 12a). The trapping of the photogenerated holes by ammonium oxalate might suppress the recombination of the photoinduced electron-hole pairs. Hence, more Cr(VI) ions could be reduced with the photogenerated electrons of B_4C [1].

The initial pH of the Cr(VI) solution has a significant effect on the Cr(VI) photoreduction reaction. To reveal the effect of the initial pH of the Cr(VI) solution, the current pH of the Cr(VI) solution was changed to about 4 and 10 with HCl or NaOH, respectively. When the initial pH of the Cr(VI) solution was 4, the Cr(VI) photoreduction rate of B_4C(5,2.5) increased from 65.15 to 71.9% within 120 min (Fig. 12b). On the other hand, the Cr(VI) photoreduction rate of B_4C(5,2.5) decreased to 58.0% when the initial pH of the Cr(VI) solution was 10 (Fig. 12b). It was reported by that the acidic environment was beneficial for the adsorption of Cr(VI) by the photocatalyst, while the alkaline environment was not favorable for the adsorption of Cr(VI) [1]. In addition, the reaction mechanism studies exhibited that the acidic environment was also beneficial for the photoreduction of Cr(VI) [1].

In order to study the effect of the initial Cr(VI) concentration on the photoreduction efficiency of B_4C, $K_2Cr_2O_7$ concentration of the solution was changed to 10 and 30 mg/l, respectively. By reducing the $K_2Cr_2O_7$ concentration of the solution to 10 mg/l, the Cr(VI) photoreduction efficiency of B_4C(5, 2.5) increased slightly to 67.1% (Fig. 12c). In contrast, increasing the $K_2Cr_2O_7$ concentration of the solution to 30 mg/l slightly reduced the Cr(VI) photoreduction efficiency to 63.2% (Fig. 12c). In dilute solution, an increase in the light intensity reaching the photocatalyst surface is expected. When the photocatalyst concentration is kept constant, a higher rate of the incoming light can be absorbed by B_4C in a dilute solution, leading to an increase in the charge carrier density required for the Cr(VI) photoreduction. In this respect, the reduction in the Cr(VI) photoreduction efficiency with the increase in the initial Cr(VI) concentration can be attributed to the low absorption of the incident light by B_4C(5,2.5).

According to Fig. 12d, the Cr(VI) photoreduction efficiency enhanced with increasing the photocatalyst concentration, which was attributed to the fact that an increase in the photocatalyst concentration can supply more active sites for the Cr(VI) photoreduction reaction [2]. When the B_4C(5,2.5) concentration was adjusted to be 0.1 and 10 g/l, the Cr(VI) photoreduction efficiency changed to 35.1 and 72.5%, respectively. The recyclability of B_4C was also studied. The Cr(VI) removal rate of B_4C(5,2.5) reduced from 65.1 to 52.4% after four consecutive cycles of the Cr(VI) photoreduction experiments (Fig. 12e). The slight decrease in the Cr(VI) photoreduction efficiency might be assigned to the residual Cr(VI) and Cr(III) ions adsorbed on the active sites of the photocatalyst [57].

9 Conclusion

B_4C powders were successfully synthesized and applied for the Cr(VI) removal from aqueous solution using the photoreduction process. The results of the Cr(VI) removal experiments revealed that visible light was more effective in the Cr(VI) photoreduction process. The presence of the B_4C seed crystals and the Ni catalyst might increase the nucleating points during the crystal growth and results in the formation of smaller crystallite structures with high crystal purity. The crystal purity of the as-prepared product influenced the Cr(VI) photoreduction efficiency. Within the scope of the present study, the potential for use of B_4C as a photocatalyst was studied, and the Cr(VI) photoreduction efficiency of B_4C, prepared in the presence of the B_4C seed crystals and the Ni catalyst, was enhanced. The photoinduced electrons exhibited the active role in the visible light driven photoreduction of Cr(VI). The Cr(VI) photoreduction efficiency of B_4C decreased about 13% after four cycles within 120 min. The acidic solution medium was beneficial for the Cr(VI) photoreduction. Higher Cr(VI) removal was obtained when the initial photocatalyst concentration was increased and the initial Cr(VI) concentration was decreased.

Supplementary Information The online version contains supplementary material available at https://doi.org/10.1007/s43207-023-00307-3.

Author contributions All authors contributed to the study conception and design. Material preparation, data collection and analysis were performed by OK and HNK. The first draft and the revised draft of the manuscript were written by OK and HNK. They read and approved the final manuscript.

Funding This research has been supported by The Scientific and Technological Research Council of Turkey (TÜBİTAK) with the Project Number 120M005.

Data availability The data that support the findings of this study are available from the corresponding author upon reasonable request.

Declarations

Conflict of interest The authors declare no competing interests. The authors have no relevant financial or non-financial interests to disclose.

References

1. H.F. Yin, C.Y. Yuan, H.J. Lv, K.Y. Zhang, X. Chen, Y.Z. Zhang, Ceram. Int **48**(8), 11320 (2022)
2. L.X. Li, H.J. Gao, G.R. Liu, S.F. Wang, Z. Yi, X.W. Wu, H. Yang, Adv. Powder Technol. **33**(3), 103481 (2022)

3. H.Y. Xu, Y.C. Yang, D.C. Li, R.R. Wu, A.G. Wang, D.S. Sun, F.J. Zhang, W.C. Oh, J. Korean Ceram. Soc. (2022). https://doi.org/10.1007/s43207-022-00224-x
4. C. He, B. Zhang, Y. Jiang, H. Liu, H.P. Zhao, Chem. Eng. J. **403**, 126429 (2021)
5. R. Verma, P.K. Maji, S. Sarkar, J. Ind. Eng. Chem. **111**, 147 (2022)
6. S.A. Jadhav, H.B. Garud, S.S. Thoravat, V.S. Patil, P.S. Shinde, S.H. Burungale, P.S. Patil, Biointerface Res. Appl. Chem. **11**(2), 8599 (2021)
7. S. Rezgui, M. Ghazouani, L. Bousselmi, H. Akrout, J. Environ. Chem. Eng. **10**(3), 107424 (2022)
8. J.H. Ou, Y.T. Sheu, D.C.W. Tsang, Y.J. Sun, C.M. Kao, Chemosphere **256**, 127158 (2020)
9. S. Roy, S. Majumdar, G.C. Sahoo, S. Bhowmick, A.K. Kundu, P. Mondal, J. Hazard. Mater. **399**, 122841 (2020)
10. G. Dong, L. Zhang, J. Phys. Chem. C **117**(8), 4062 (2013)
11. M. Canterino, I. Di Somma, R. Marotta, R. Andreozzi, Water Res. **42**, 4498 (2008)
12. Z.P. Guo, W. Wei, Y.H. Li, Z.Y. Li, F.M. Hou, A. Wei, J. Hazard. Mater. **422**, 126946 (2021)
13. L.H. Xu, J. Su, G.G. Zheng, L. Zhang, Mater. Sci. Eng. B-Adv Funct. Solid-State Mater. **248**, 114405 (2019)
14. H. Ullah, T. Balkan, I.S. Butler, S. Kaya, Z.U. Rehman, J. Coord. Chem. **74**(9–10), 1628 (2021)
15. D. Hu, C. Song, X. Jin, Q. Huang, J. Alloys Compd. **843**, 156030 (2020)
16. F.E.B. Coelho, V.M. Candelario, A.E.M. Rodrigues, M.T.L. Santos, G. Magnacca, Nanomaterials **10**(4), 779 (2020)
17. M. Jafarzadeh, ACS Appl. Mater. Interfaces **14**(22), 24993 (2022)
18. E. Ersoz, O.A. Yildirim, J. Korean Ceram. Soc. **59**(5), 655 (2022)
19. D.L. Hernandez-Arellano, J.C. Duran-Alvarez, S. Cortes-Lagunes, R. Zanella, T.E. Soto, R. Lopez-Juarez, J. Korean Ceram. Soc. **60**(1), 113 (2022)
20. P. Singh, G. Kaur, K. Singh, M. Kaur, M. Kumar, R. Meena, R. Bala, A. Kumar, Materialia **1**, 258 (2018)
21. Y.V. Bogatov, V.A. Shcherbakov, A.E. Sychev, Inorg. Mater. **58**(5), 525 (2022)
22. O. Coban, M. Bugdayci, M.E. Acma, J. Aust Ceram. Soc. **58**(3), 777 (2022)
23. D. Kozien, I. Czekaj, M. Ziabka, M. Bik, K. Pasiut, D. Zientara, Z. Pedzich, Adv. Eng. Mater. **24**(9), 2101795 (2022)
24. X. Li, M.J. Lei, S.B. Gao, D. Nie, K. Liu, P.F. Xing, S. Yan, Int. J. Appl. Ceram. Technol. **17**(3), 1079 (2020)
25. A.L. Ortiz, F. Sanchez-Bajo, V.M. Candelario, F. Guiberteau, J. Eur. Ceram. Soc. **37**(13), 3873 (2017)
26. M. Zhu, X.Y. Hu, Y.N. Wei, Y.J. Zhang, X.W. Du, X.Z. Zhang, J. Cryst. Growth **311**(14), 3721 (2009)
27. A. Aghaie, C. Falamaki, B.E. Yekta, M.S. Afarani, Ind. Ceram. **22**(2), 121 (2002)
28. B.S. Kozekanan, A. Moradkhani, H. Baharvandi, N. Ehsani, J. Korean Ceram. Soc. **59**(2), 180 (2021)
29. K.H. Kim, J.H. Chae, J.S. Park, D.K. Kim, K.B. Shim, B.H. Lee, J. Korean Ceram. Soc. **45**(1), 60 (2008)
30. P.H. Li, M.D. Ma, Y.J. Wu, X. Zhang, Y.K. Chang, Z.W. Zhuge, L. Sun, W.T. Hu, D.L. Yu, B. Xu, J. Eur. Ceram. Soc. **41**(7), 3929 (2021)
31. Y. Sun, K.L. Chintersingh, M. Schoenitz, E.L. Dreizin, J. Phys. Chem. C **123**(18), 11807 (2019)
32. I. Yanase, R. Ogaware, H. Kobayashi, Mater. Lett. **63**, 91 (2009)
33. S. Mondal, A.K. Banthia, J. Eur. Ceram. Soc. **25**, 287 (2005)
34. N. Shawgi, S.X. Li, S. Wang, Ceram. Int. **43**(13), 10554 (2017)
35. M. Kakiage, N. Tahara, S. Yanagidani, I. Yanase, H. Kobayashi, J. Ceram. Soc. Japan **119**, 422 (2011)
36. R.M. da Rocha, F.C.L. de Melo, Mater. Sci. Forum **660–661**, 948 (2010)
37. D.J. Yan, J.K. Liu, X.C. Fu, P.L. Liu, H.A. Luo, J. Mater. Sci. **54**, 6151 (2019)
38. A. Lace, D. Ryan, M. Bowkett, J. Cleary, Int. J. Environ. Res. Public. Health **16**(10), 1803 (2019)
39. N. Doufar, M. Benamira, H. Lahmar, M. Trari, I. Avramova, M.T. Caldes, J. Photochem. Photobiol A-Chem **386**, 112105 (2020)
40. H.V. SarithaDevi, M.S. Swapna, S. Sankararaman, J. Mater. Sci. : Mater. Electron **32**, 7391 (2021)
41. J. Park, S. Her, S. Cho, S.M. Woo, S. Bae, Cem. Concr Compos. **129**, 104458 (2022)
42. X.W. Chen, S.M. Dong, Y.M. Kan, H.J. Zhou, J.B. Hu, Y.S. Ding, RSC Adv. **6**(11), 9338 (2016)
43. H.V. SarithaDevi, M.S. Swapna, G. Ambadas, S. Sankararaman, Chin. Phys. B **27**(10), 107702 (2018)
44. D. Jasrotia, B. Singh, A. Kumar, S.K. Verma, P.A. Alvi, K. Kumar, B. Sridhar, Results Phys. **14**, 102421 (2019)
45. L.Y. Zhao, X.L. Dong, J.Y. Chen, A.H. Lu, Chem-Eur. Ji **26**(9), 2041 (2020)
46. H.F. Yin, T.L. Fan, Y. Cao, P.F. Li, X.X. Yao, X.H. Liu, J. Hazard. Mater. **420**, 126567 (2021)
47. S. Challagulla, R. Nagarjuna, R. Ganesan, S. Roy, ACS Sustain. Chem. Eng. **4**(3), 974 (2016)
48. X.J. Zhang, L. Wang, Q.C. Du, Z.Y. Wang, S.G. Ma, M. Yu, J. Colloid Interface Sci. **464**, 89 (2016)
49. C.M. Khor, M.M. Khan, M.Y. Khan, A. Khan, M.H. Harunsani, Chem. Phys. Impact **4**, 100082 (2022)
50. C. Sakthivel, A. Nivetha, G. Thiruppathi, P. Sundararaj, I. Prabha, New. J. Chem. **47**(2), 571 (2023)
51. A.M. Oda, H.H. Ali, A.J. Lafta, H.A. Esmael, A.A. Jameel, A.A. Mohammed, I. Mubarak, Int. J. Chem. **7**, 39 (2015)
52. R. Saravanan, F. Gracia, A. Stephen, in *Nanocomposites for Visible Light-Induced Photocatalysis*, ed. by M.M. Khan, D. Pradhan,Y. Sohn. Springer Series on Polymer and Composite Materials, vol101(Springer,Switzerland,2017)
53. W.L. Cen, T. Xiong, C.Y. Tang, S.D. Yuan, F. Dong, Ind. Eng. Chem. Res. **53**(39), 15002 (2014)
54. A.M. Palve, J. Alloys Compd. **868**, 159143 (2021)
55. Y.F. Lv, Y. Liu, J. Wei, M.Y. Li, D.Y. Xu, B. Lai, Chem. Eng. J. **417**, 129188 (2021)
56. K. Villa, J.R. Galan-Mascaros, Chemsuschem **14**, 2023 (2021)
57. X.G. Zheng, T.T. Liu, J. Wen, X.H. Liu, Chemsphere **278**, 130422 (2021)